

# INTERCHANGE RECONNECTION FORCED BY THE FILAMENT ERUPTION INSIDE A PSEUDO-STREAMER

JIAYAN YANG<sup>1</sup>, YUNCHUN JIANG<sup>1</sup>, ZHE XU<sup>1,2</sup>, YI BI<sup>1</sup>, AND JUNCHAO HONG<sup>1</sup>

<sup>1</sup>Yunnan Observatories, Chinese Academy of Sciences, P.O. Box 110, Kunming 650011, China; [yjy@ynao.ac.cn](mailto:yjy@ynao.ac.cn)

<sup>2</sup>Graduate School of Chinese Academy of Sciences, Beijing 100049, China

Received 2014 September 4; accepted 2015 February 13; published 2015 April 17

## ABSTRACT

We present rare observational signatures of interchange reconnection (IR) forced by the filament eruption inside a pseudo-streamer (PS). The PS was centered above a positive-polarity region bounded by two negative-polarity coronal holes (CHs), and thus its base contained two polarity inversion lines and a pair of loop arcades where two filaments were harbored. In white-light coronagraph data from two different views, it showed up as a fan-shaped structure consisting of fine rays and a coronal streamer. Followed by a two-ribbon flare and a coronal mass ejection, one of the filaments and its overlying arcade erupted away from the nearby CH and flew over the other arcade to interact with the PS's remote CH. As a result, distinct ribbon-like remote brightenings formed along the remote CH boundary and were connected to the positive-polarity flare ribbon by a loop system, but the nearby open-field region largely remained unchanged except that compact brightenings and a following small coronal dimming appeared close to one end of the erupted filament. In combination with the coronal magnetic configuration that derived from the potential-field source-surface model, these observations can be interpreted as follows: the erupting field was first deflected and guided by the nearby CH's open field and then reconnected with the oppositely oriented open field of the remote CH, during which both the closed field bridging the erupted filament and the remoter CH's open field were transported in the opposite direction. The observations thus supported the idea that PSs provide favorable environments for IR to take place and remote brightenings along their CH boundaries represent a credible IR signature on the solar surface.

**Key words:** Sun: activity – Sun: coronal mass ejections (CMEs) – Sun: filaments, prominences – Sun: flares – Sun: magnetic fields

**Supporting material:** animation

## 1. INTRODUCTION

Magnetic reconnection between open and closed fields, a process known as interchange reconnection (IR; Crooker et al. 2002), can lead to an interchange of the closed field and a transfer or jump of the open field, during which the closed-field line opens up while the open-field line closes down, with the conservation in the total amount of open and closed flux. As a common underlying mechanism, IR has been suggested to play crucial roles in a broad form of coronal and heliospheric phenomena, such as the evolution of coronal holes (CHs) and their boundaries (Wang & Sheeley 2004; Fisk 2005; Baker et al. 2007; Edmondson et al. 2010; Kahler et al. 2010; Yokoyama & Masuda 2010; Antiochos et al. 2011; Titov et al. 2011), the recovery and recurrence of coronal dimmings associated with coronal mass ejections (CMEs; Attrill et al. 2008; Krista & Reinard 2013), the circulation and reversal of the global magnetic field and the regulation of the interplanetary magnetic field strength (Fisk & Schwadron 2001; Crooker et al. 2002; Owens & Crooker 2006; Lavraud et al. 2011), the generation of the slow solar wind from closed-field regions (Schwadron et al. 1999; Neugebauer & Liewer 2003; Lionello et al. 2005; Del Zanna 2008; van Driel-Gesztelyi et al. 2012; Riley & Luhmann 2012; Wang et al. 2012), and so on.

A suitable environment for IR to occur requires that magnetic loops of various sizes can expand to interact with the ambient open fields. Regarding the existence of an open- and closed-field boundary as a basic necessary condition, several special magnetic configurations that are highly favorable for IR have been discussed before. When magnetic bipoles

or active regions (ARs) emerge inside CHs or at CH boundaries (Shibata et al. 1994; Ma et al. 2014), IR between them often leads to the formation of “sea anemone” structures (Asai et al. 2008; Baker et al. 2009; Lugaz et al. 2011) and the trigger of solar jets (Madjarska et al. 2004; Doyle et al. 2006; Pariat et al. 2009; Yang et al. 2011). An erupting closed-field structure, such as a CME loop from a flare or a filament eruption, stands a chance to meet with an open field of nearby or remote CHs and thus can possibly drive IR. There are two possibilities determined by the relative orientation of the closed and open fields (Gopalswamy et al. 2009). When the fields are parallel, the closed-field structure will only be guided and thus deflected by the open field. When the fields are antiparallel, however, IR between them is possible. It is reported that filament eruptions or CMEs can disturb nearby CHs (Hudson et al. 1996; Thompson et al. 1998; Vršnak et al. 2003; Liu et al. 2009; Gutiérrez et al. 2013), and some observations have suggested that, regarding brightenings along CH boundaries as a signature, IR might take place between an erupting structure and a CH (Sterling & Moore 2001; Attrill et al. 2006; Crooker & Webb 2006; Harra et al. 2007; Cohen et al. 2010).

Coronal streamers have also long been acknowledged to favor the development of IR, and it is now well accepted that these features can be classified into two fundamentally different categories (Hundhausen 1972; Wang et al. 2007a, 2007b). (1) Bipolar or helmet streamers overlie a single (or an odd number of) polarity inversion line (PIL) or loop arcade bounded by open fields of opposite polarity, with a cusp or Y-type neutral point well above  $2 R_{\odot}$  as the origin of the heliospheric current sheet between the two open-field domains. (2) Unipolar streamers or pseudo-streamers (PSs) overlie two (or an even

number of) PILs/loop arcades bounded by open fields of like polarity, such that the two open-field domains converge above the closed-field regions to form a low-lying cusp coinciding with an X-type null point (NP) well below  $2 R_{\odot}$ , without a current sheet in the outer corona. In upper-coronal white-light coronagraph observations, both types of streamers consist of radial fine rays, which have been thought to be the result of quasi-steady IR occurring at their cusps and to represent open-field lines with relatively enhanced electron density. When viewed at different orientations, these rays can form bright long stalks or fainter and broader fan-shaped features, but both types of streamers show similar morphologies in appearance and are often indistinguishable from one another. However, several recent studies showed that magnetic field and EUV observations near the solar surface can truly distinguish PSs from helmet streamers by their double-lobed bases (Pasachoff et al. 2011; Seaton et al. 2013; Masson et al. 2014; Rachmeler et al. 2014).

Like helmet streamers, PSs are commonplace above activity-complex and quiet regions of the solar surface (Eselevich et al. 1999; Wang et al. 2007b; Masson et al. 2014) and over the entire solar cycle (Seaton et al. 2013). Because the double-arcade systems of a PS can occasionally harbor two filaments and the lower height of its cusp likely results in a more rapid decrease in field strength with height (Rachmeler et al. 2014), it appears that a PS configuration is prone to producing not only a single filament eruption (Wang et al. 2009; Zuccarello et al. 2012; Bi et al. 2013) but also sympathetic twin filament eruptions (Török et al. 2011; Titov et al. 2012; Lynch & Edmondson 2013; Panasenco et al. 2013). While a gradual and quasi-steady IR process at the cusp of a PS has been proposed to be responsible for the long-lasting evolution and dynamics of its white-light and EUV structures (Wang et al. 2007b; Masson et al. 2014), it is naturally expected that filament eruptions from a PS will induce quicker and more explosive IR and show clear signatures and drastic changes along the involved CH boundaries. On 2012 September 9, a filament and its overlying arcade underwent an eruption inside a PS with double arcades bounded by two like-polarity CHs. While the nearby open-field region was nearly unaffected, the filament erupted toward another arcade of the PS to approach and interact with the remote CH. As a result, distinct remote brightenings appeared along the CH boundary. Taken such brightenings as a credible IR signature, this event allows us to detail the eruption dynamics and the sequent IR process.

## 2. INSTRUMENTATION

The 2012 September 9 event was well covered by the observations from the Atmospheric Imaging Assembly (AIA; Lemen et al. 2012) and the Helioseismic and Magnetic Imager (HMI; Scherrer et al. 2012) on board the *Solar Dynamics Observatory* (SDO; Pesnell et al. 2012), as well as the Global Oscillation Network Group (GONG) at the National Solar Observatory (NSO). AIA takes full-disk images in 10 UV and EUV wavelengths covering a wide range of temperatures with a pixel size of  $0''.6$  at high cadence up to 12 s. We use the Level 1.5 304, 171, 193, and 211 Å images to study the event. The 304 Å (He II;  $\log T = 4.7$ ) and 171 Å (Fe IX;  $\log T = 5.8$ ) are mainly formed in the chromosphere and transition region, 193 Å (Fe XII;  $\log T = 6.1$ ) mainly reveals information of the corona and is also sensitive to 20 MK plasma (Fe XXIV), while 211 Å (Fe XIV;  $\log T = 6.3$ ) is sensitive in response to the flaring

or active-region corona. HMI makes measurements of full-disk line-of-sight magnetic fields in the Fe I absorption line at 6173 Å with a spatial sampling of  $0''.5 \text{ pixel}^{-1}$ , a cadence of 45 s, and a precision of 10 G. GONG provides full-disk H $\alpha$  images with a pixel size of  $1''$  and a cadence of 1 minute. Finally, the associated coronal structures are also examined using full-disk soft X-ray (SXR) images with a several-hour cadence from the X-Ray Telescope (XRT) aboard the *Hinode* satellite (Kosugi et al. 2007).

The event was also observed by the Extreme Ultraviolet Imager (EUVI; Wuelser et al. 2004) on board the *Solar Terrestrial Relations Observatory* (STEREO-A; Kaiser et al. 2008) spacecraft, which provides full-disk 304 Å images for the event, with a field of view (FOV) out to about  $1.5 R_{\odot}$ , a pixel size of  $1''.6$ , and a cadence of 10 minutes. On 2012 September 9, STEREO-A was about  $124^\circ$  ahead of the Earth, and thus the eruptive region in the southwestern quadrant of the solar disk as viewed by SDO was close to the east limb as viewed by STEREO-A. To identify the associated white-light coronal structures and CME, we utilized observations from the inner (COR1) and outer (COR2) coronagraphs aboard STEREO-A (Howard et al. 2008), with FOVs of  $1.4\text{--}4.0 R_{\odot}$  and  $2.0\text{--}15.0 R_{\odot}$ , respectively. We also examined the C2 white-light coronagraph data that cover the range  $2\text{--}6 R_{\odot}$  from the Large Angle and Spectrometric Coronagraphs (LASCO; Brueckner et al. 1995) aboard the *Solar and Heliospheric Observatory* (SOHO). All the data are processed by using standard software programs in the SolarSoftWare (SSW), and then AIA, HMI, GONG, and XRT data are differentially rotated to a reference time close to the event.

## 3. OBSERVATIONS

The eruptive filament, “F,” was located to the southeast of AR 11568 (S  $15^\circ$  W  $23^\circ$ ) and centered at about S  $25^\circ$ , W  $15^\circ$ . Figure 1 shows the general appearances of the eruptive region before the eruption in the AIA 193 Å image (panel (a)) and HMI magnetogram (panel (b)). In the AIA 193 Å image, we see two CHs: a small one, “CH1,” and a more extensive one, “CH2.” Between them, there were two EUV filament channels. According to the H $\alpha$  image in the following Figure 2, there were indeed two filaments embedded in these filament channels: the eruptive filament F was in the eastern thin channel, and another filament, “F1,” was in the western diffuse channel. The corresponding HMI magnetogram showed that the eruptive region had a “negative–positive–negative” polarity distribution from northeast to southwest and thus covered two distinct PILs. When we superimposed the outlines of the 193 Å CH1 and CH2, the pre-eruptive H $\alpha$  axes of F and F1, and two dimming regions “DB” and “RB” that occurred during the F eruption on the HMI magnetogram, it became clear that CH1, CH2, DB, and RB were predominantly located over negative-polarity unipolar regions, while F and F1 were along the two PILs between the two CHs of the same polarity. Such a magnetic-field setting might be associated with a PS (Wang et al. 2007b), and we will describe this point in more detail below. Here the CH boundaries are only estimated visually owing to the difficulty of their exact determination, the axes of F and F1 are determined from the H $\alpha$  image of Figure 2, and the outlines of DB and RB are also determined from Figure 2.

Figure 2 further shows the eruptive region before and after the eruption in GONG H $\alpha$  and AIA 304 Å images. Panels (a1)

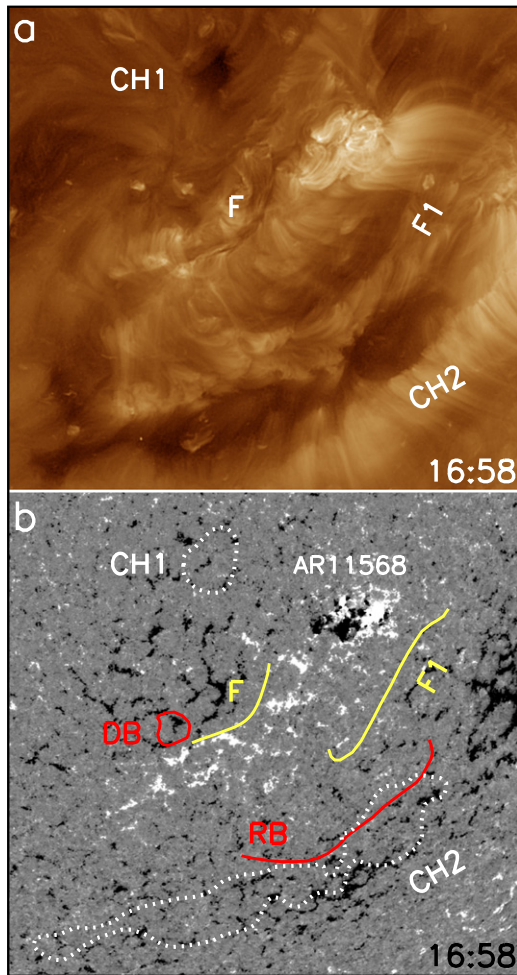


**Figure 1.** (a) AIA 193 Å direct image and (b) HMI magnetogram showing the general appearance of the eruptive region before eruption. Two filaments, “F” and “F1,” are located between two like-polarity coronal holes, “CH1” and “CH2.” “DB” and “RB” are two brightenings that occurred after the F eruption; see also the accompanying animation. The axis outlines of F and F1 from panel (a1) of Figure 2, the visual-determined boundaries of CH1 and CH2 from panel (a), and the rough outlines of DB and RB from panel (b2) of Figure 2 are all plotted in the HMI magnetogram to show their relative positions clearly. The FOV is  $672'' \times 636''$ .

and (b1) show the state of pre-eruption, while (a2) and (b2) show that of post-eruption. We see that F was clearly visible in the first  $H\alpha$  image (panel (a1)), but most of the filament was not visible in the second one (panel a2), while F1 was left almost unchanged. Although no *GOES* flare was recorded, as a normal feature of filament eruptions, the F eruption was accompanied by a typical two-ribbon flare on its opposite sides (panels a2 and b2). However, the most remarkable characteristic of the eruption is the appearance of remote brightenings RB along CH2’s northern boundary and well separated from the flare site. Similar remote brightenings at CH’s boundaries were also observed in some previous events (Sterling & Moore 2001; Attrill et al. 2006; Crooker & Webb 2006; Liu et al. 2006). In the 304 Å fixed-base difference image (panel b2) after the eruption, RB can be clearly seen as a bright ribbon longer than the flare ribbons. Moreover, like endpoint brightenings in some erupting filaments (Wang et al. 2009), more compact brightenings DB also appeared close to F’s south-eastern end. DB connected but did not completely belong to the

flare’s left ribbon, and it is easy to distinguish them from each other. Clearly, RB and DB were not the results of spreading and expansion of the flare ribbons, and thus they should have different origins.

## 4. RESULTS

### 4.1. Eruption

The detailed F eruption process is shown by representative AIA 304 and 193 Å images in Figure 3, as well as the six-panel movie with AIA 304 Å, fixed-base difference AIA 304 Å, AIA 193 Å, fixed-base difference AIA 193 Å,  $H\alpha$ , and HMI magnetograms, named “2012.0909.mpeg,” available in the online journal. Obviously, F erupted bodily toward the southwestern direction, and its top headed for CH2 (panel (a1)), during which F did not show any direct interaction with CH2. This is different from the case shown by Jiang et al. (2007b), in which a filament first erupted toward, then met with, and finally was deflected back by a remote CH. However, the consequent RB along CH2’s boundary, occurring nearly simultaneously with the flare and DB (panels (a2) and (b1)), indeed indicated that CH2 was disturbed by the erupting filament-carrying fields. It is also noted that CH1 was unaffected by the eruption. Afterwards, the two flare ribbons separated away from each other and EUV post-eruptive loops gradually appeared to connect them (panels (a3) and (b2)), RB and DB slowly faded away, and as indicated by the white arrows, a small coronal dimming region, “D,” developed adjacent to DB. Fortunately, XRT provided an SXR image at the later phase of the eruption (panel (c)). Besides the SXR post-eruptive loops with strong emission, a faint loop system, “L,” appeared to connect positive-polarity regions near the flare and negative-polarity regions close to RB. In previous remote brightenings along CH boundaries (Sterling & Moore 2001; Attrill et al. 2006; Crooker & Webb 2006), similar SXR loops were also observed to extend from flare-core regions to remote brightening regions.

### 4.2. Consequences of Eruption

Because the most striking difference of the event from typical filament eruptions is the appearance of RB and DB, their detailed morphologic evolutions should contain important information to understand their origin. This is illustrated by the close-up view of AIA EUV and HMI observations in Figures 4 and 5. Figure 4 shows DB’s evolution. As indicated by the black arrow in panel b1, there were coronal loops connecting opposite-polarity magnetic patches around DB before the eruption (panels (a) and (b1)). Consistent with the previous result that the formation of coronal dimmings might be preceded by brightenings (Jiang et al. 2007a; Yang et al. 2012), DB’s occurrence (panel (c1)) was followed by D’s formation along its northern side (panels (c2) and (c3); see also the AIA 304 and 193 Å difference panels in the movie) and the disappearance of the loops (panel (b2)). D was located over the negative-polarity footpoint region of the disappeared loops and thus probably represented the evacuated feet of these loops due to their expansion or even opening (Jiang et al. 2008).

RB’s evolution was displayed in Figure 5. Like small-scale unresolved patchy bright chains in EIT crinkles (Sterling & Moore 2001), RB showed its first signal as a bright compact patch consisting of small bright points (panels (b1) and (d1)).



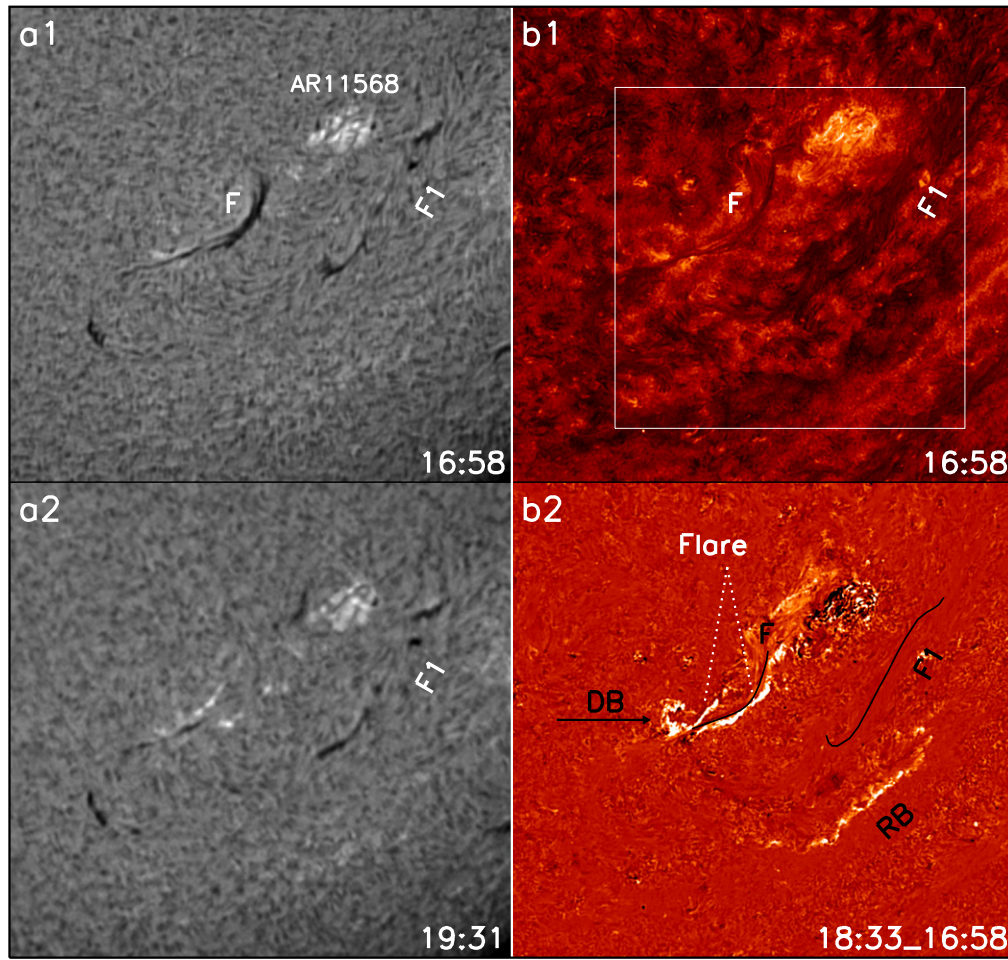


**Figure 2.** (a1)–(a2) GONG  $H\alpha$ , (b1) AIA 304 Å direct, and (b2) fixed-base difference images. (a1) and (b1) show the state of pre-eruption, while (a2) and (b2) show that of post-eruption. After the F eruption, two places brightened besides a flare with two ribbons at its two sides. The compact brightenings, “DB,” appeared at its southeastern end, and the ribbon-like remote brightenings, “RB,” appeared far away from the flare site along the northern boundary of CH2 (see also the accompanying animation). All these features are overlaid in the magnetogram of Figure 1. The FOV is the same as that of Figure 1, and the white box in (b1) indicates the FOV of Figure 3.

(An animation of this figure is available.)

Then RB extended along CH2’s boundary to form a continuous bright ribbon that was more extensive at 304 Å than at 193 Å (panels (b2), (b3), (d2), and (d3); see also the accompanying animation). Meanwhile, RB also intruded into CH2 obviously. As indicated by the dashed fiducial lines along a local smooth CH2 boundary (panels (c) and (d1)–(d3)), the major part of RB penetrated into CH2 from its left side and thus led to an obvious retraction of the CH2 boundary. This RB evolution quite resembled that of the long bright streak at the north-polar CH boundary in the 1997 May 12 event (Thompson et al. 1998; Attrill et al. 2006; Crooker & Webb 2006). By carefully examining AIA observations, furthermore, no EUV wave was found to be associated with the F eruption, and thus we can exclude the possibility that RB was caused by interaction between Moreton or/and EUV waves and CH2 (Veronig et al. 2006). Summarily, these observations imply that IR between the erupting field of F and the open field of CH2 should be responsible for the production of RB, DB, D, and L, and CH2’s retraction should be caused by a discontinuous transfer or jump of its open field to the opposite site of the erupting F (Vršnak et al. 2003; Attrill et al. 2006; Crooker & Webb 2006).

To comprehensively display the entire process of the event from the F eruption through the DB and RB formation, time slices along a slit, “S,” indicated by the long white arrows in Figure 3, are constructed from AIA 304 and 193 Å images. S passes DB, D, the left leg of the erupting F1, the two flare ribbons, RB, and CH2 and thus can reflect their spatial and temporal relationship more clearly. Figure 6 presents the results, along with the light curves of AIA 304, 171, 193, and 211 Å intensities in the flare, RB, and D. We can see that F showed up as dark streaks in the time slices and had two distinct motion stages: a slow rise phase and a sudden eruption phase (panels (a) and (b)). The application of linear fittings to the rising/erupting dark streaks gives average speeds of  $1.5/52.1 \text{ km s}^{-1}$ , and their intersect defines the start time of the F eruption at about 17:54 UT, immediately followed by the occurrences of the separating flare ribbons, RB, DB, and D. It is noted that F1 seemed not to be affected by the passage of F, and RB had brightened before F reached the CH2 boundary. To detail the shrinkage of the CH2 boundary due to RB’s intrusion, a smaller region enclosing RB (the dotted box in panel (b)) is selected and shown (panels (c) and (d)). Clearly, RB appeared as a straight bright streak, penetrating into CH2

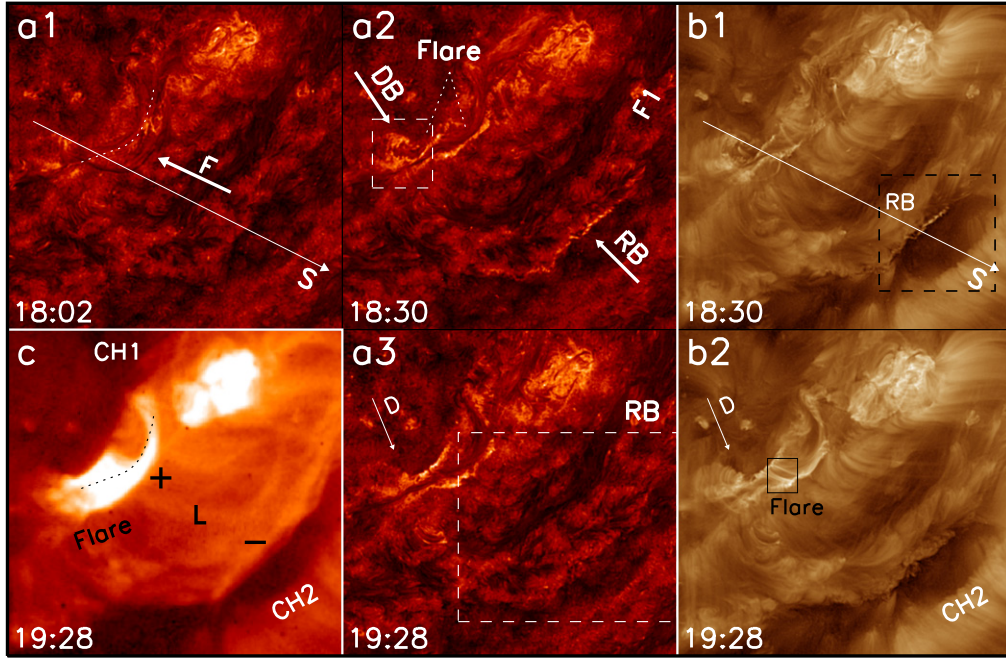


**Figure 3.** AIA (a1)–(a3) 304 and (b1), (b2) 193 Å, and (c) *Hinode*/XRT SXR images showing the F eruption. The axis outlines of F in the 16:58 UT H $\alpha$  image are plotted as dotted curves in (a1) and (c), and the plus/minus signs in (c) mark the corresponding photospheric positive/negative polarities. The white long arrows, “S,” indicate the slit position of the time slices shown in Figure 6; the solid box in (b2) marks the area, in which EUV light curves of the flare are measured and displayed in Figure 6; the dashed box in (a2) indicates the FOV of Figure 4, and the other two dashed boxes in (a3)/(b1) indicate the FOVs of the top/bottom rows in Figure 5. After the F erupted bodily, the flare and DB occurred near its original location, while RB occurred along CH2’s boundary almost at the same time, showing the signal of the interaction between F and CH2. A small coronal dimming “D” appeared later near DB, and a faint SXR loop system “L” gradually connected the flare region and RB region. The FOV is  $468'' \times 456''$ .

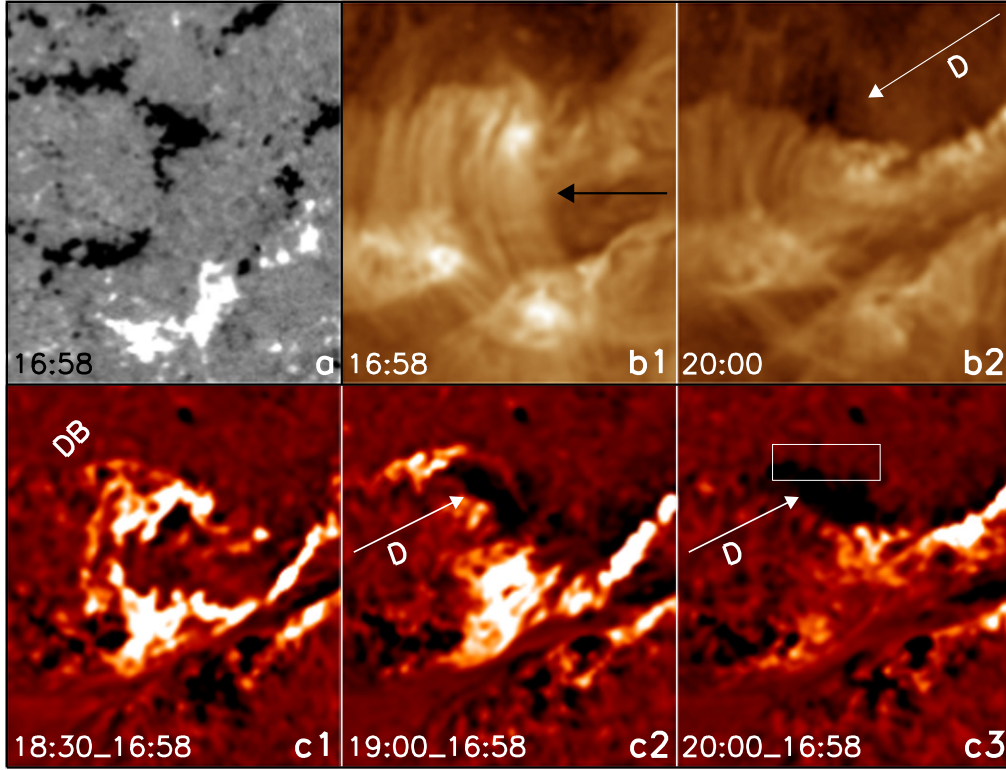


**Figure 4.** Close-up view of DB’s evolution in (a) HMI magnetogram, (b1), (b2) AIA 195 Å direct, and (c1)–(c3) 304 Å fixed-base difference images. The black arrow in (b) indicates coronal loops that connected opposite-polarity magnetic patches around DB before F eruption and disappeared after the eruption. The white arrows indicate a small coronal dimming, “D,” forming along the northern side of DB (see also the accompanying animation). The solid boxes in (c3) mark the area in which the EUV light curve of D is measured and displayed in Figure 6. The FOV is  $84'' \times 96''$ .



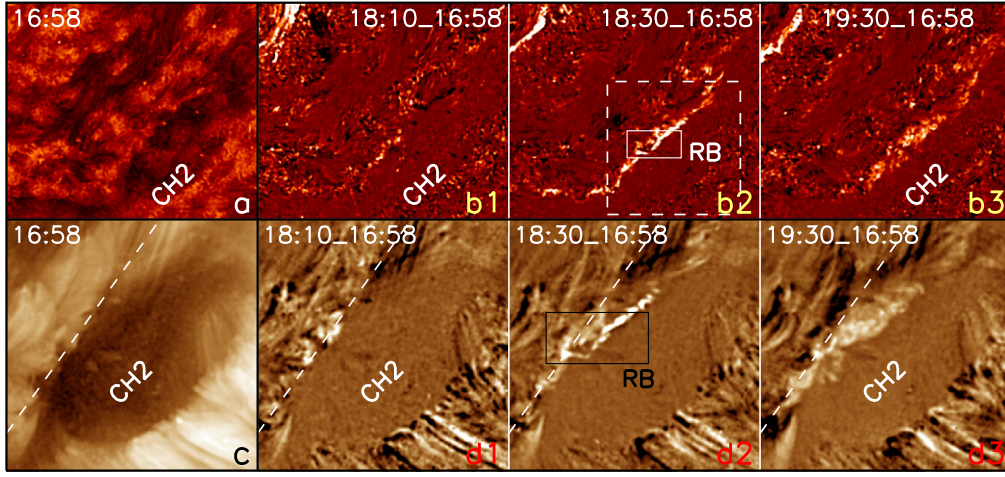


**Figure 5.** Close-up view of RB's evolution in (a) AIA 304 and (c) 195 Å direct, and (b1), (b3) AIA 304 and (d1)–(d3) 195 Å fixed-base difference images. RB appeared as a continuous bright ribbon along CH2's northeastern boundary. The dashed lines in (c) and (d1)–(d3) indicate the roughly smooth boundary of CH2, and it is obviously that the major part of RB penetrated into CH2 during its evolution. The solid boxes in (e2) and (g2) mark the area in which the EUV light curve of RB is measured and displayed in Figure 6. The dashed box in (b2) indicates the FOV of the bottom row. The FOVs are  $306'' \times 264''$  for the top row and  $162'' \times 162''$  for the bottom row.

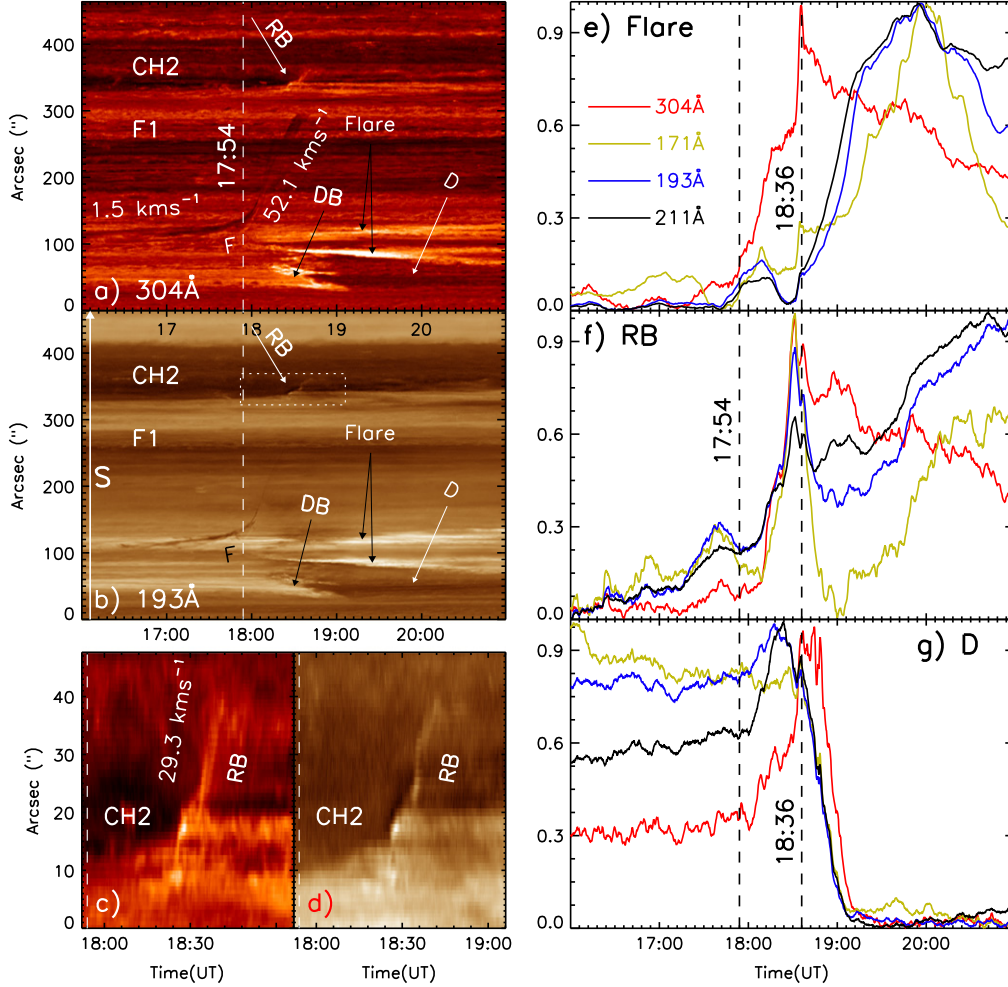


**Figure 6.** Time slices from AIA (a) 304 and (b) 193 Å images for the slit S depicted in Figure 3, and close-up view of a smaller region surrounding RB indicated by the dotted box in (b) at (c) 304 and (d) 193 Å, with the white dashed vertical lines indicating the start time of the F eruption at 17:54 UT. The light curves of AIA 304, 171, 193, and 211 Å intensities are shown as a function of time in areas centered on (e) the flare, (f) RB, and (g) D indicated by the solid boxes in Figures 3–5. The light curves are computed from the intensity integrated and normalized over the areas. The start time of the F eruption and the peak time of the flare are indicated by the black dashed vertical lines. The light curves show that the flare, RB, and D regions had obvious emission enhancements after the F eruption and almost simultaneously reached the peak values at 18:36 UT, indicating that these phenomena should relate to each other tightly.

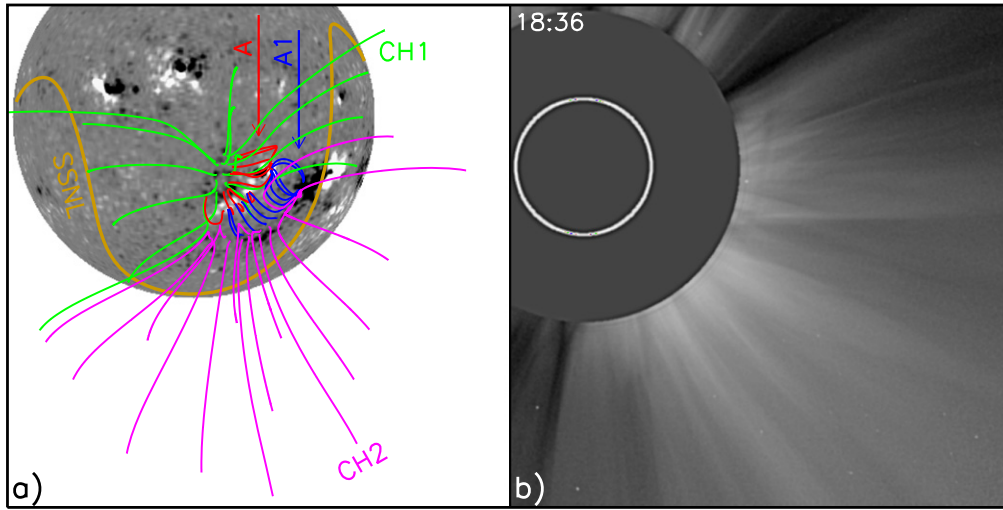


**Figure 7.** (a) PFSS coronal field-line configuration close to the eruptive region. Open-field lines directed inward and anchored in negative-polarity regions around CH1/CH2 are coded in green/pink. For clarity, only closed-field lines extending lower than  $1.2 R_{\odot}$  are selected, and those consisting of two loop arcades, “A/A1,” which hold F/F1, are coded in red/blue. The brown curve, “SSNL,” is the projection of the source surface neutral line. Such a magnetic topology indicates the existence of a PS. (b) LASCO C2 white-light image over the eruptive region at the time close to the event.

with an estimated average speed of  $29.3 \text{ km s}^{-1}$  by a linear fitting. The light curves indicate that, after the F eruption at 17:54 UT, the flare, RB, and D regions had obvious emission enhancements at four lines forming in a large temperature range from several  $10^4 \text{ K}$  to a few  $10^6 \text{ K}$  (panels (e)–(g)). Probably as a result of the appearance of the flare arcade lagging that of the flare ribbons (see Figure 2), the  $304 \text{ \AA}$  flare peak time of about 18:36 UT preceded those at the other wavelengths. However, the brightenings of RB and D at four lines almost simultaneously peaked at about 18:36 UT, implying that these phenomena should have a tight temporal relationship. After this peak time, the intensities in D decreased sharply at all the measured wavelengths, indicating that the formation of D was probably due to a density loss instead of a temperature decrease of the coronal plasma (Attrill et al. 2006; Jiang et al. 2008).

#### 4.3. Potential-field Source-surface Modeling

As mentioned above, the eruptive region might be associated with a PS covering the two CHs, and thus the knowledge of large-scale magnetic configuration should be crucial for the clarification of this point. Since CHs are considered as the footpoints of open magnetic field lines, the potential-field source-surface (PFSS) modeling is appropriate for the identification of such a configuration (Schrijver & DeRosa 2003; Wang et al. 2007a, 2007b; Liu et al. 2009). Using the PFSS software package available in SSW, which is based on the PFSS model of the Schrijver & DeRosa (2003) and synoptic magnetic maps from HMI, the ambient large-scale magnetic topology was obtained. We used the synoptic map at the time closest to the event studied here, and only the open-field lines from the regions around CH1/CH2 and closed-field lines over the original F and F1 were selected. Figure 7 presents the result (panel (a)) and compares it with a corresponding LASCO C2 white-light image (panel (b)). As expected, two arcades, “A/A1,” consisting of red/blue closed-field lines appear to overlie the two PILs and F/F1. It seems that the green/pink open-field lines emanating from the negative-polarity CH1/CH2 and neighboring regions converge above

the closed-field regions. Such a field-line topology is a typical property of PSs (Wang et al. 2007b). When the projection of the computed source-surface neutral line (SSNL) down onto the photospheric magnetogram is plotted as the brown curve, we see that A/A1 and CH1/CH2 are located on its left side, i.e., SSNL’s projection does not pass through the closed-field regions. Because SSNL is identified with the cusp of a helmet streamer belt at  $2.5 R_{\odot}$ , where the radial field is set to zero (Smith 2001), the eruptive region should coincide with the double-lobed base of a PS adjacent to a helmet streamer. In line with the previous observations (Wang et al. 2007a; Masson et al. 2014), a fan-shaped white-light structure appeared above the southwestern limb (panel (b)). It consisted of some fine ray-like features, which might have resulted from interchange and slipping reconnections of closed and open fields with a long-lasting and quasi-steady nature. Because the axes of A/A1 and the nearby SSNL’s projection are oriented nearly parallel rather than perpendicular to the sky plane, it is very likely that a face-on PS was observed against the background of a face-on helmet streamer.

#### 4.4. Deflected Eruption and CME

Although LASCO data showed no CME in association with the event, a CME from the F eruption was actually observed to be along a preexisting streamer from the view of *STEREO-A*. This is shown in Figure 8. The F eruption was obvious in EUVI-A  $304 \text{ \AA}$  images after 17:54 UT (panels (a1)–(a4)). Embedded in the green open-field lines from CH1, F did not rise radially but erupted toward the southeastern direction and so approached the converging cusp of the green/pink open-field lines from CH1/CH2 (panel (b)). Therefore, it is very likely that the erupting F was deflected and guided by the open field of CH1 (Gopalswamy et al. 2009). Before the CME, there was a diffuse bright feature above the erupting F in the COR1-A FOV (panel (b)), but a northeast-oriented long stalk-like streamer, “Str,” was clearly revealed by the COR2-A observations (panel (c)). Very similar to previous white-light PS observations (Wang et al. 2007b; Liu et al. 2009), Str was probably the edge-on outward extension beyond  $2.0 R_{\odot}$  of the



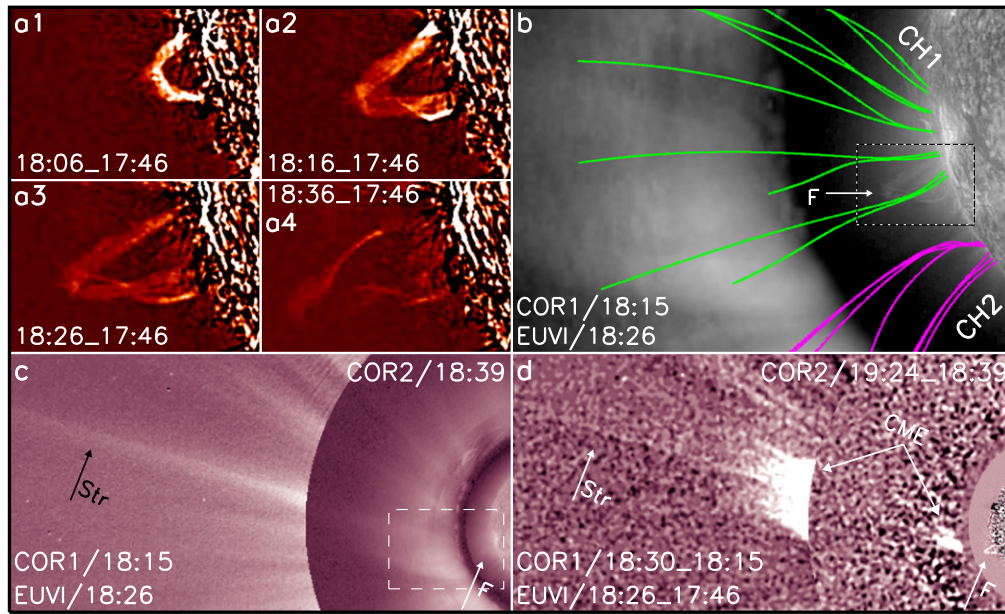


**Figure 8.** (a1)–(a4) *STEREO-A/EUVI* 304 Å fixed-base difference images showing the erupting F. The FOV is  $397'' \times 270''$ . (b) Composite image of direct *STEREO-A/EUVI* 304 Å and COR1 images overlaid by the extrapolated open-field lines from CH1 (green) and CH2 (pink). The FOV is  $1.77 R_{\odot} \times 1.22 R_{\odot}$ , and the dashed box indicates the FOV of panels (a1)–(a4). Composite image of (c) direct and (d) fixed-base difference *STEREO-A/EUVI* 304 Å, COR1, and COR2 images showing a coronal streamer, “Str,” overlying the erupting F and a CME along Str after the F eruption. It is noticed that the final direction of the CME deflected from that of the erupting F obviously. The FOV is  $7.71 R_{\odot} \times 3.96 R_{\odot}$ , and the dashed box in (c) indicates the FOV of (b).

PS base identified in the *SDO* observations. As shown in the composite image made from difference EUVI-A 304 Å, COR1-A, and COR2-A images at different instances (panel (d)), moreover, the CME indeed originated from the F eruption and had a northeastern trajectory along Str. This further make us believe that F actually erupted inside a PS. Note that the erupting F had a great difference in orientation from the final CME, supporting that CHs should play a role in deflecting CMEs at their initial eruption phase (Panasenco et al. 2013).

## 5. INTERPRETATION AND DISCUSSION

The above observations suggest that the erupting F inside the PS was first deflected by CH1 and then reconnected with CH2. To better understand the IR process, Figure 9 presents the close-up view of the PS base in a pre-eruptive HMI magnetogram, superposing with the PFSS extrapolated coronal field lines and the outlines of F, F1, CH1, CH2, RB, and DB. As described above, the PS base shows a “negative-positive-negative” tripolar magnetic nature. F/F1 along the two PILs share the same positive-polarity region and are bridged by the red/blue A/A1 arcades, which are sandwiched between the green/pink CH1/CH2 open fields. While the pink field lines are mainly connected to CH2, the green ones anchor on not only CH1 but also the nearby negative-polarity region. Clearly, DB is adjacent to the interface between A and the green field lines, and RB is almost coincident with the footpoints of the pink field lines along the CH2 boundary. As a typical signature of PSs, the green/pink field lines converge as a cusp above A/A1, where a magnetic NP should be formed. To clarify whether an NP is associated with the PS, the PFSS model should include more accurate information provided by the available observations. Because the potential field in the PFSS model matches a global photospheric radial field that can be obtained by the observed line-of-sight magnetograms being assimilated into a flux-dispersal model (Schrijver & DeRosa 2003), the global

radial field calculated from the synoptic map is inserted with the HMI magnetogram at 16:58 UT and used as the bottom boundary for the PFSS model (Bi et al. 2013), and then the trilinear null finding method of Haynes & Parnell (2007) is used to scan the PFSS-modeled field. As expected (Wang et al. 2007b), a low-lying NP is determined to locate  $0.09 R_{\odot}$  above the solar surface between A and A1 (see the black plus sign). Consistent with previous results (Panasenco et al. 2013), the F eruption was roughly guided toward this NP.

A series of phenomena accompanied the filament eruption, such as the flare, brightenings (RB and DB), coronal dimming (D), coronal loops, etc. To make the eruption process clearer, Table 1 summarized the occurring time of these main characters. Combining the PFSS extrapolation with the observations, RB, DB, and D can be naturally explained as a consequence of IR between the magnetic fields of the erupting F and CH2. The sequence of cartoons presented in Figure 10 depicts our interpretation of the event, in which only a few representative field lines are drawn and the erupting F is simply indicated by the solid black circles. The initial PS configuration includes red/blue arcades A/A1 that hold F/F1 and are located between the green/pink open fields from like-polarity CH1/CH2 (panel (a)). After the F eruption starts (panel (b)), F and A are deflected and guided by the green open field and thus rise and expand to approach the NP. As the closed external loops of A meet with the pink open field, IR, i.e., external reconnection, occurs between them, accompanied by internal reconnection in the interior of the expanding loops of A (Sterling & Moore 2001). The outcome of the reconnections is shown in panel (c). The internal reconnection produces the flare with two ribbons in the lower atmosphere, while the IR exchanges the connectivity between the reconnected pink open fields of CH2 and red closed fields of A to produce DB and RB, during which the pink open fields have been closed to form L, as seen in the XRT SXR image, but the red closed loops have been opened to



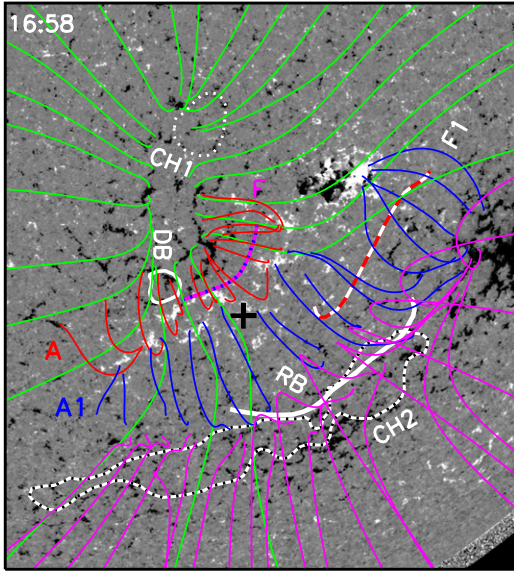


**Figure 9.** Overlay of a pre-eruptive HMI magnetogram with the extrapolated coronal field lines. This figure is the close-up view of Figure 7(a), along with superposed outlines of F, F1, CH1, CH2, RB, and DB, to show the temporal correlations of all the features of this event in the context of magnetic field. The two CHs are separated by the red/blue arcades A/A1, which hold F/F1. Open-field lines directed inward are coded in green/pink for those connecting to CH1/CH2 and their nearby regions, respectively. The thick black plus sign marks the site of the NP determined by using a trilinear method of Haynes & Parnell (2007) to model the PFSS field, confirming the typical magnetic topology of PS. The FOV is  $696'' \times 770''$ .

**Table 1**

Time of the Main Characters Occurring in the Filament Eruption

The start time of the F eruption	17:54 UT
The initial time of flare, RB and DB	Immediately after 17:54 UT
The peak time of flare, RB and DB	18:36 UT
The start time of the D formation	After 18:36 UT

form D. The consequence of this process is equivalent to an interchange of the red closed field and a jump of the pink open field in opposite directions across the NP over a distance spanning A and A1. Clearly, the progressing IR can generate the observational characteristics that RB only showed pure brightenings intruding into CH2 owing to the greater involvement of CH2's pink open-field lines, while the DB brightenings

were followed by the nearby D owing to the greater opening of A's red closed-field lines. Finally, the joint effect of the internal reconnection and IR is the formation of an escaping "plasmoid," which explodes outward along PS's open lines to produce the CME. Overall, such a simple scenario can well explain all of the main phenomena observed in this event and thus should capture the most important aspect of the event. It is worthwhile to point out that, in the 1998 May 1–2 and 1997 May 12 events, which were independent of any PS configuration, a similar scenario for IR driven by filament eruptions was also proposed to explain EIT crinkles and remote EUV brightenings along CH's boundaries (Sterling & Moore 2001; Attrill et al. 2006; Crooker & Webb 2006).

This event is strongly supportive of the idea that PS configurations are favorable for IR to occur between open and closed fields. Comprehensively considering IR events observed up to now, it appears that remote brightenings along CH boundaries indicate a reliable signature for IR regardless of whether a PS is involved or not. To our best knowledge, however, our event offers the first distinct low-corona evidence for IR forced by a filament eruption in a PS. Like explosive IR in jets occurring between open fields and newly emerging fields, the filament-eruption-driven IR also has an impulsive nature as compared with the gradual IR processes in long-lasting, quasi-steady EUV and white-light PS structures (Wang et al. 2007a, 2007b; Seaton et al. 2013; Masson et al. 2014). Because PSs are commonplace in the Sun (Eselevich et al. 1999; Masson et al. 2014) and CMEs from filament eruptions inside PSs are also not uncommon (Wang et al. 2009; Panasenco et al. 2013), similar to the case of the gradual IR, impulsive IR driven by filament eruptions should occur frequently in PSs, and relevant remote brightenings along their CH boundaries should be common phenomena. Clearly, more observations are needed to further clarify such a possibility. In particular, a PS is also appropriate to sympathetic twin filament eruptions from its double arcades (Lynch & Edmondson 2013). In such a case, IR should occur in each eruption, and thus remote twin brightenings should sequentially appear at the inner boundaries of its two CHs. Because only the 2010 August 1–2 event was reported and simulated until recently (Schrijver & Title 2011; Török et al. 2011; Titov et al. 2012; Panasenco et al. 2013), however, it is unclear whether such remote twin brightenings can be really observed in sympathetic eruptions from a PS. The F eruption in the present event did not induce a

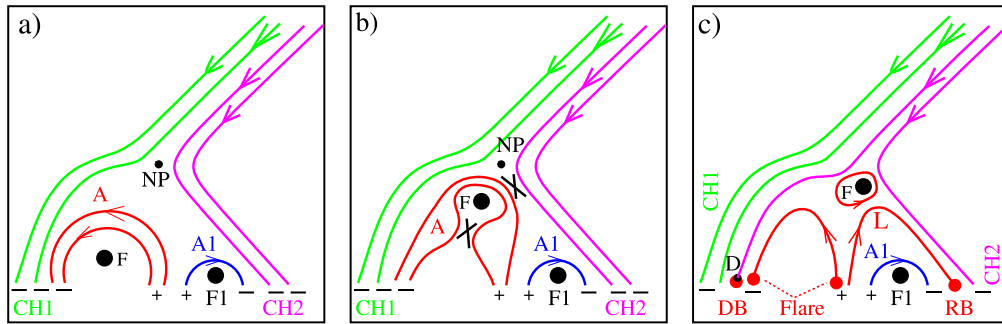


**Figure 10.** Sketch illustrating IR between the erupting F and CH2. The green/pink open-field lines from CH1/CH2 and the red/blue closed-field lines of A/A1 are plotted. The arrows indicate the field directions; the elongated crosses label the sites of the internal reconnection and IR; the plus/minus signs mark the photospheric positive/negative polarities; the black filled circles indicate F, F1, NP, and D; and the red filled circles indicate the two flare ribbons, RB, and DB. (a) Initial PS configuration before eruption. Two filaments are held by two coronal arcades sandwiched between two like-polarity coronal holes, and an NP exists between the arcades. (b) Magnetic configuration during the eruption. F rises deflected and pushes A to approach the NP, and then IR takes place between A and open field lines, and internal reconnection occurs inside the expanding A. (c) After the connection. The flare is the outcome of internal reconnection, the escaping F is the joint outcome of internal reconnection and IR, while the dimming region D, the SXR loop system L shown in Figure 3(c), and two brightenings DB and RB are all from the IR.

following F1 eruption in a few days by tracking the evolution of the eruptive region using AIA observations, but sympathetic eruptions from a PS accompanied by remote twin brightenings were found by seeking recent *SDO* observations, and a study will be given in a separate paper to detail this question.

We thank an anonymous referee for many constructive suggestions and thoughtful comments that improved the quality of this paper. The authors thank the *SDO*, *Hinode*, and *SOHO*/LASCO teams, as well as the GONG/NSO and *STEREO* consortia, for granting free access to their Internet databases. *Hinode* is a Japanese mission developed and launched by ISAS/JAXA, with NAOJ as domestic partner and NASA and STFC (UK) as international partners. It is operated by these agencies in cooperation with ESA and NSC (Norway). This work is supported by the 973 Program (2011CB811403) and by the Natural Science Foundation of China under grants 11473065, 11273056, and 11333007.

## REFERENCES

- Antiochos, S. K., Mikić, Z., Titov, V. S., Lionello, R., & Linker, J. A. 2011, *ApJ*, **731**, 112
- Asai, A., Shibata, K., Hara, H., & Nitta, N. V. 2008, *ApJ*, **673**, 1188
- Attrill, G., Nakwacki, M. S., Harra, L. K., et al. 2006, *SoPh*, **238**, 117
- Attrill, G., van Driel-Gesztelyi, L., Démoulin, P., et al. 2008, *SoPh*, **252**, 349
- Baker, D., Rouillard, A. P., van Driel-Gesztelyi, L., et al. 2009, *AnGeo*, **27**, 3883
- Baker, D., van Driel-Gesztelyi, L., & Attrill, G. 2007, *AN*, **328**, 773
- Bi, Y., Jiang, Y., Yang, J., et al. 2013, *ApJ*, **773**, 162
- Brueckner, G. E., Howard, R. A., Koomen, M. J., et al. 1995, *SoPh*, **162**, 357
- Cohen, O., Attrill, G. D. R., Schwadron, N. A., et al. 2010, *JGR*, **115**, A10104
- Crooker, N. U., Gosling, J. T., & Kahler, S. W. 2002, *JGR*, **107**, 1028
- Crooker, N. U., & Webb, D. F. 2006, *JGR*, **111**, A08108
- Del Zanna, G. 2008, *A&A*, **481**, 49
- Doyle, J. G., Popescu, M. D., & Taroyan, Y. 2006, *A&A*, **446**, 327
- Edmondson, J. K., Antiochos, S. K., DeVore, C. R., Lynch, B. J., & Zurbuchen, T. H. 2010, *ApJ*, **714**, 517
- Eselevich, V. G., Fainshtein, V. G., & Rudenko, G. V. 1999, *SoPh*, **188**, 277
- Fisk, L. A. 2005, *ApJ*, **626**, 563
- Fisk, L. A., & Schwadron, N. A. 2001, *ApJ*, **560**, 425
- Gopalswamy, N., Mäkelä, P., Xie, H., Akiyama, S., & Yashiro, S. 2009, *JGR*, **114**, A00A22
- Gutiérrez, H., Taliashvili, L., & Mouradian, Z. 2013, *AdSpR*, **51**, 1824
- Harra, L. K., Crooker, N. U., Mandrini, C. H., et al. 2007, *SoPh*, **244**, 95
- Haynes, A. L., & Parnell, C. E. 2007, *PhPI*, **14**, 2107
- Howard, R. A., Moses, J. D., Vourlidas, A., et al. 2008, *SSRv*, **136**, 67
- Hudson, H. S., Acton, L. W., & Freeland, S. L. 1996, *ApJ*, **470**, 629
- Hundhausen, A. 1972, *Coronal Expansion and Solar Wind* (Berlin: Springer)
- Jiang, Y., Shen, Y., Bi, Y., Yang, J., & Wang, J. 2008, *ApJ*, **677**, 699
- Jiang, Y., Yang, L., Li, K., & Ren, D. 2007a, *ApJL*, **662**, L131
- Jiang, Y., Yang, L., Li, K., & Shen, Y. 2007b, *ApJL*, **667**, L105
- Kahler, S., Jibben, P., & DeLuca, E. E. 2010, *SoPh*, **262**, 135
- Kaiser, M. L., Kucera, T. A., Davila, J. M., et al. 2008, *SSRv*, **136**, 5
- Kosugi, T., Matsuzaki, K., Sakao, T., et al. 2007, *SoPh*, **243**, 3
- Krista, L. D., & Reinard, A. 2013, *ApJ*, **762**, 91
- Lavraud, B., Owens, M. J., & Rouillard, A. P. 2011, *SoPh*, **270**, 285
- Lemen, J. R., Title, A. M., Akin, D. J., et al. 2012, *SoPh*, **275**, 17
- Lionello, R., Riley, P., Linker, J. A., & Mikić, Z. 2005, *ApJ*, **625**, 463
- Liu, C., Lee, J., Deng, N., Gary, D. E., & Wang, H. 2006, *ApJ*, **642**, 1205
- Liu, Y., Luhmann, J. G., Lin, R. P., et al. 2009, *ApJL*, **698**, L51
- Lugaz, N., Downs, D., Shibata, K., et al. 2011, *ApJ*, **738**, 127
- Lynch, B. J., & Edmondson, J. K. 2013, *ApJ*, **764**, 87
- Ma, L., Qu, Z.-Q., Yan, X.-L., & Xue, Z.-K. 2014, *RAA*, **14**, 221
- Madjarska, M. S., Doyle, J. G., & van Driel-Gesztelyi, L. 2004, *ApJL*, **603**, L57
- Masson, S., McCauley, P., Golub, L., Reeves, K. K., & DeLuca, E. E. 2014, *ApJ*, **787**, 145
- Neugebauer, M., & Liewer, P. C. 2003, *JGR*, **108**, A11013
- Owens, M. J., & Crooker, N. U. 2006, *JGR*, **111**, A10104
- Panasenco, O., Martin, S. F., Velli, M., & Vourlidas, A. 2013, *SoPh*, **287**, 391
- Pariat, E., Antiochos, S. K., & DeVore, C. R. 2009, *ApJ*, **691**, 61
- Pasachoff, J. M., Rušin, V., Druckmüllerová, H., et al. 2011, *ApJ*, **734**, 114
- Pesnell, W. D., Thompson, B. J., & Chamberlin, P. C. 2012, *SoPh*, **275**, 3
- Rachmeler, L. A., Platten, S. J., Bethge, C., Seaton, D. B., & Yeates, A. R. 2014, *ApJL*, **787**, L3
- Riley, P., & Luhmann, J. G. 2012, *SoPh*, **277**, 355
- Scherrer, P. H., Schou, J., Bush, R. I., et al. 2012, *SoPh*, **275**, 207
- Schrijver, C. J., & DeRosa, M. L. 2003, *SoPh*, **212**, 165
- Schrijver, C. J., & Title, A. M. 2011, *JGR*, **116**, A04108
- Schwadron, N. A., Fisk, L. A., & Zurbuchen, T. H. 1999, *ApJ*, **521**, 859
- Seaton, D. B., de Groof, A., Shearer, P., Berghmans, D., & Nicula, B. 2013, *ApJ*, **777**, 72
- Shibata, K., Nitta, N., Strong, K. T., et al. 1994, *ApJL*, **431**, L31
- Smith, E. J. 2001, *JGR*, **106**, 15819
- Sterling, A. C., & Moore, R. L. 2001, *ApJ*, **560**, 1045
- Thompson, B. J., Plunkett, S. P., Gurman, J. B., et al. 1998, *GeoRL*, **25**, 2461
- Titov, V. S., Mikić, Z., Linker, J. A., Lionello, R., & Antiochos, S. K. 2011, *ApJ*, **731**, 111
- Titov, V. S., Mikić, Z., Török, T., Linker, J. A., & Panasenco, O. 2012, *ApJ*, **759**, 70
- Török, T., Panasenco, O., Titov, V. S., et al. 2011, *ApJL*, **739**, L63
- van Driel-Gesztelyi, L., Culhane, J., Baker, D., et al. 2012, *SoPh*, **263**, 135
- Veronig, A. M., Temmer, M., Vršnak, B., & Thalmann, J. K. 2006, *ApJ*, **647**, 1466
- Vršnak, B., Warmuth, A., Maričić, D., Otruba, W., & Ruždjak, V. 2003, *SoPh*, **217**, 187
- Wang, Y.-M., Biersteker, J. B., Sheeley, N. R., Jr., et al. 2007a, *ApJ*, **660**, 882
- Wang, Y.-M., Grappin, R., Robbrecht, E., & Sheeley, N. R., Jr. 2012, *ApJ*, **749**, 182
- Wang, Y.-M., Muglach, K., & Kliem, B. 2009, *ApJ*, **699**, 133
- Wang, Y.-M., & Sheeley, N. R., Jr. 2004, *ApJ*, **612**, 1196
- Wang, Y.-M., Sheeley, N. R., Jr., & Rich, N. B. 2007b, *ApJ*, **658**, 1340
- Wuelser, J.-P., Lemen, J. R., Tarbell, T. D., et al. 2004, *Proc. SPIE*, **5171**, 111
- Yang, J., Jiang, Y., Bi, Y., et al. 2012, *ApJ*, **749**, 12
- Yang, S., Zhang, J., Li, T., & Liu, Y. 2011, *ApJL*, **732**, L7
- Yokoyama, M., & Masuda, S. 2010, *SoPh*, **263**, 135
- Zuccarello, F. P., Bemporad, A., Jacobs, C., et al. 2012, *ApJ*, **744**, 66